Nanoscale Advances

ROYAL SOCIETY OF CHEMISTRY

PAPER

View Article Online
View Journal | View Issue

Cite this: *Nanoscale Adv.*, 2025, **7**, 517

A high stretchability fiber based on a synergistic three-dimensional conductive network for wide-range strain sensing†

Wei Shi,‡[a] Xing Yang,‡[a] Langhuan Lei,‡[a] Xiaozhi Huang,[b] Jiali Lin,[a] Qiuyu Liang,[a] Wei Li*[b] and Jianrong Yang *[a]

Fiber strain sensors are promising for constructing high-performance wearable electronic devices due to their light weight, high flexibility and excellent integration. However, the conductivity of most reported fiber strain sensors is severely degraded, following deformation upon stretching, and it is still a considerable challenge to achieve both high conductivity and stretchability. Herein, we have fabricated a fiber strain sensor with high conductivity and stretchability by integrating the AgNPs into the multi-walled carbon nanotube/graphene/thermoplastic polyurethane (MWCNT/GE/TPU) fiber. The tunneling-effect dominated MWCNT/GE layer bridges separated AgNP islands, endowing conductive fibers with the integrity of conductive pathways under large strain. By means of the synergistic effect of a three-dimensional conductive network, the fiber strain sensor of AgNPs/MWCNT/GE/TPU presents not only a high conductivity of 116 S m^{-1}, but also a wide working range of up to 600% and excellent durability (8000 stretching-releasing cycles). Remarkably, benefiting from the crack propagation on the brittle AgNP layer, the fiber strain sensor exhibits a large resistance change in the strain range of 500–600%, and thus high sensitivity with a gauge factor of 545. This fiber strain sensor can monitor human physiological signals and body movement in real-time, including pulse and joint bending, which will contribute to the development of smart textiles and next-generation wearable devices.

Received 15th September 2024
Accepted 23rd November 2024

DOI: 10.1039/d4na00770k

rsc.li/nanoscale-advances

1. Introduction

Flexible strain sensors play an important role in the fields of soft robotics, health monitoring, and human body motion tracking.[1–5] Compared with film strain sensors, fiber strain sensors have higher compliance to irregular surfaces of the human body, and superior breathability for air, moisture and body liquids.[6–8] Specifically, it is also easily integrated into yarns, fabrics and clothing, which is compatible with the idea of seamless human–machine integration. Therefore, the fiber is an ideal platform for wearable and stretchable strain sensing systems.[9,10]

Generally, there are mainly two typical methods to endow stretchable fibers with conductivity, according to the manner of constructing the conductive network on the surface or inside the fiber. The first method is to coat or deposit conductive materials on the surface of a stretchable fiber.[11–13] Although the initial conductivity of these conductive fibers is high, the poor adhesion between the fiber matrix and the conductive layer, resulting in poor stability against external mechanical stimulations, greatly limits the wide application of fiber strain sensors.[7,14] The second method is to construct conductive composite fibers. Compared with the method of coating, the interface bonding between conductive materials and the fiber matrix in conductive composite fibers is often stronger, and the constructed conductive network has stable and firm characteristics. Among them, carbon-based (carbon black (CB)[15,16] carbon nanotubes (CNTs),[17–19] and graphene (GE)[20,21]) fillers have been widely employed in a variety of composite fibers due to their excellent electrical conductivity. In general, conductive composite fibers face contradiction between conductivity and stretchability, *i.e.*, the addition of conductive fillers can improve the conductivity of the fibers, while high volume fraction conductive fillers can reduce the stretchability of the fibers.[14,22] Therefore, it is still a challenge to fabricate fiber strain sensors with both high conductivity and excellent stretchability. The construction of synergistic conductive network has been proved to be an effective method to fabricate fiber strain sensors with both high conductivity and excellent stretchability.[23–26] For example, Lee *et al.*[27] reported a fiber strain sensor with AgNWs

[a]*Health Management Research Institute, People's Hospital of Guangxi Zhuang Autonomous Region, Guangxi Academy of Medical Sciences, Nanning, 530021, People's Republic of China. E-mail: liwei2186gxqyy@163.com; jianguansuo2024YJR@163.com*

[b]*Health Management Center, People's Hospital of Guangxi Zhuang Autonomous Region, Guangxi Academy of Medical Sciences, Nanning, 530021, People's Republic of China*

† Electronic supplementary information (ESI) available. See DOI: https://doi.org/10.1039/d4na00770k

‡ These authors contributed equally to this work.

and a AgNP synergistic conductive network, displaying high conductivity (2450 S m^{-1}) and stretchability (900% strain). Therefore, this will be a promising strategy to integrate the concept of a synergistic conductive network into fiber strain sensors.

In this study, we developed a three-dimensional (0D–1D–2D) synergistic conductive network composed of 0D Ag nanoparticles (AgNPs), 1D multi-wall carbon nanotubes (MWCNTs) and 2D GE by wet spinning and *in situ* reduction methods, which provides the AgNPs/MWCNT/GE/TPU (AMGT) fiber with high conductivity (116 S cm^{-1}). Specifically, the MWCNT/GE layer can bridge the separate AgNP islands, so that the conductive fiber can maintain conductivity under large strain (wide operating range of 0–600%). Moreover, the developed AMGT fiber strain sensor has high sensitivity (GF of 545) and significant durability (8000 stretching-releasing cycles). At last, the fiber strain sensor has been successfully applied to the detection of human pulse signals and body movement. The three-dimensional synergistic conductive fiber holds great promise for smart fabrics and wearable devices.

2. Experimental section

2.1. Materials

Thermoplastic polyurethanes (TPU, Elastollan C80A) used as the matrix material for this work were obtained from BASF Co. Ltd. *N*,*N*-Dimethylformamide (DMF), isopropanol (IPA) and ethanol were purchased from Shanghai Richjoint Chemical Reagent Co., Ltd (Shanghai, China). Ag acetate ($AgCF_3COO$) and hydrazine hydrate ($N_2H_4 \cdot 4H_2O$, ≈50–60%) were provided by Innochem Technology Co., Ltd (Beijing, China). The multi-walled carbon nanofibers (MWCNTs, purity > 95 wt%) with a diameter of 5 to 15 nm and length of 10–30 μm and graphene (GE, layer <3) with a diameter <10 μm and thickness of 1–3 nm were purchased from XFNANO Co., Ltd (Nanjing, China). All the chemicals were analytical grade reagents and were used as received without further purification.

2.2. Fabrication of MWCNT/GE/TPU fibers

First, MWCNTs and GE are added to DMF at a certain mass ratio and dispersed by using an ultrasonic signal generator to form a stable suspension. Then, TPU was added to the suspension and stirred at 80 °C for 60 min to form a spinning solution with a mass fraction of 20 wt%. Finally, the spinning solution is squeezed into a coagulation bath composed of a mixture of ethanol and isopropanol and dried for a period of time to form MWCNT/GE/TPU fibers. The MWCNT/GE/TPU fibers were optimized by mixing with different weight ratios of the MWCNTs and GE, and the weight ratio was set to 0, 0.1, 0.3, 0.5, and 1.0, respectively.

2.3. Fabrication of AgNPs/MWCNT/GE/TPU fibers

Ag acetate was dissolved in ethanol solvent (15 wt%) and utilized as Ag precursor solutions. The MWCNT/GE/TPU fibers were immersed in the solutions for 90 min and air dried for 3 min. The reduction agents were prepared by diluting hydrazine hydrate in ethanol (1 : 1, v/v). The reduction agents were dropped onto the MWCNT/GE/TPU fibers to directly reduce the absorbed Ag ions into AgNPs in the fiber matrix. The fibers were rinsed several times with deionized water and ethanol, and air dried for 10 min.

2.4. Characterization

The structure of the fiber was studied using a field emission scanning electron microscope (FESEM, JSM-6700F, JEOL, Japan). The Fourier transform infrared spectrum (FTIR) was measured using a Fourier infrared spectrometer (Nicolet iS50). The X-ray diffraction (XRD) analysis was carried out on a diffractometer of X'Pert Pro. The samples used for these characterization studies are AMGT (where MWCNT : GE = 3 : 1) fibers. When the conductive fiber was stretched, the electrical response of the fiber was recorded by using a TEGAM 1740 microohmmeter. The R of the fiber sample is recorded by using the TEGAM 1740 micrometer and the conductivity ρ is calculated by using the following formula:

$$\rho = \frac{RS}{L} \tag{1}$$

where L (cm) represents the length of the sample and S (cm^2) represents the cross-sectional area of the sample.

The sensitivity of the strain sensor is expressed by using the gauge factor (GF) which is evaluated by using the equation:

$$\mathrm{GF} = \frac{\Delta R}{R_0} \Big/ \frac{\Delta L}{L_0} \tag{2}$$

where R_0 is the initial resistance and $\Delta R = R - R_0$ represents the relative change in resistance, and L_0 is the initial length and $\Delta L = L - L_0$ represents the relative change in length.

3. Results and discussion

3.1. Fabrication and characterization of the AMGT fiber

The conductive AMGT fiber was fabricated by wet spinning and *in situ* reduction methods, as shown in Fig. 1. Before wet spinning, the MWCNTs and GE are dispersed in TPU solution by high-speed agitation to form a spinning solution (details are listed in the Experimental section). Once the spinning solution is injected into the coagulation bath, the coagulation bath enters the interior of the incomplete solidified MWCNT/GE/TPU (MGT) fiber and occupies a certain space, due to solvent exchange. A porous structure is formed when the coagulation bath evaporates during MGT fiber drying.[28] We prepare a conductive AMGT fiber by soaking and chemical reduction methods. $AgCF_3COO$ and $N_2H_4 \cdot 4H_2O$ are used as the metal

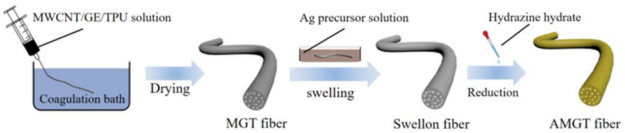

Fig. 1 Schematic illustration of the fabrication of the conductive AMGT fiber.

precursor salt and reducing agent, respectively. The through-hole structure of the MGT fiber can make Ag precursor solution and $N_2H_4 \cdot 4H_2O$ enter easily. The digital photos of MGT and AMGT fibers are shown in Fig. S1.† After the reduction process, the gray MGT fiber produces a large number of AgNPs and appears yellow. Importantly, we weaved the AMGT fiber into a fabric, showing its great application potential in smart wearable E-textiles.

To further investigate the microscopic morphologies of the AMGT fiber, the scanning electron microscopy (SEM) characterization was performed. As observed in Fig. 2a, despite a large number of AgNPs on the AMGT fiber surface, the clear pore structure can still be clearly observed, indicating that the porous structure is still well preserved after the reduction. As displayed in Fig. 2b and S2,† uniform AgNPs (average particle size of 47.89 ± 0.79 nm) are evenly distributed throughout the AMGT fiber. Besides, the AgNPs, MWCNTs and GE can be clearly seen in the interior of the AMGT fiber (Fig. 2c), and the MWCNTs and GE are located between the AgNPs, forming a three-dimensional synergistic conductive network. Due to the presence of a synergistic conductive network, especially a silver shell composed of AgNPs on the AMGT fiber surface, the AMGT fiber exhibits excellent initial conductivity ($\rho \approx 116$ S cm^{-1}). The conductivity of conductive fibers with different fillers is listed in Table S1.† To characterize these fibers at different stages, the X-ray diffraction (XRD), Fourier transform infrared (FTIR) and X-ray photoelectron spectroscopy (XPS) spectrum tests were performed on TPU, MGT and AMGT fibers, respectively (Fig. S3†). The characteristic peaks of Ag in the XRD pattern and the XPS spectrum both indicate that we have successfully synthesized AgNPs. The variation in these characteristic peaks in the FTIR results indicate that there is indeed an interaction between MWCNTs, GE and AgNPs, which is conducive to the stability of the conductive path.[28,29] Moreover, the energy dispersive spectroscopy (EDS) mapping images of the cross section of the AMGT fiber were obtained to characterize the distribution of C, Ag, and O elements, as displayed in Fig. 2d. Since the Ag precursor solution is absorbed more in the outer layer, this causes Ag to accumulate in the outer layer, while the C and O elements are evenly distributed in the AMGT fiber.

3.2. Electrical properties and the strain sensing feature of the AMGT fiber

In order to evaluate the effect of the mass ratio of MWCNTs and GE on the dispersion of fillers, the UV absorption spectra of different fillers (MWCNT : GE = 1 : 0, 3 : 1, 1 : 1, 1 : 3, 0 : 1) dispersed in *N*,*N*-dimethylformamide (DMF) solvent were obtained and are shown in Fig. S4.† When the suspended nanoparticles in DMF solvent are aggregated, they will settle and

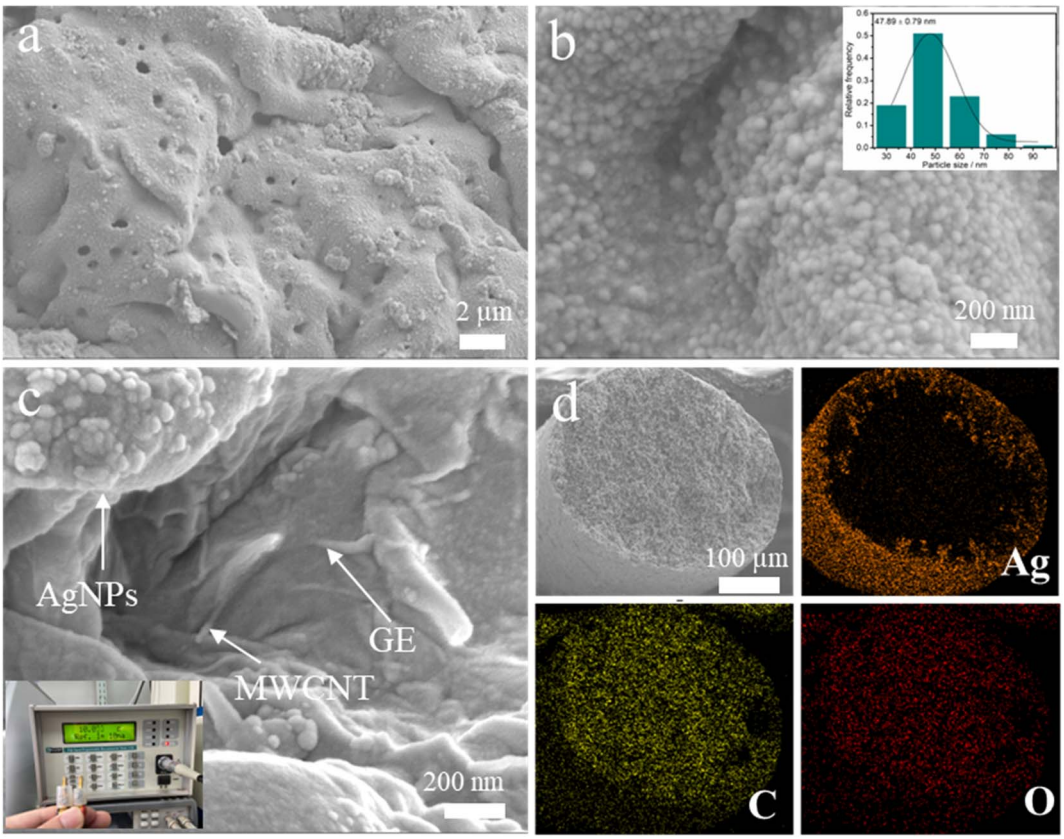

Fig. 2 (a) SEM image of the AMGT fiber surface. (b) SEM of AgNPs on the AMGT fiber surface and particle size distribution of AgNPs. (c) SEM image of the cross section of the AMGT fiber, inset shows a digital photo of the conductive fiber and *R* measurement result. (d) The SEM images of the cross section of the AMGT fiber and elemental distributions of Ag, C and O.

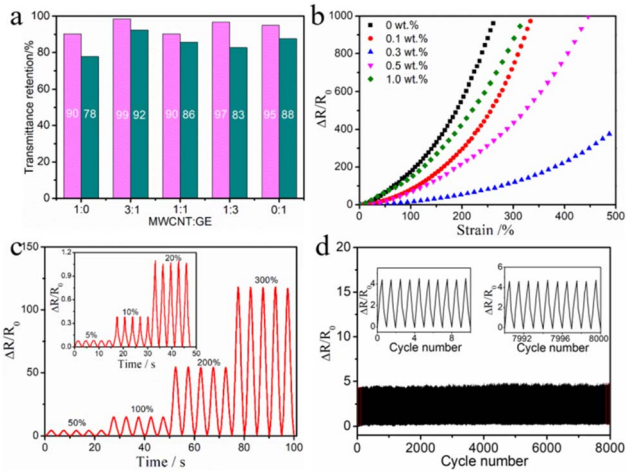

Fig. 3 (a) Statistics of the retention rate of ultraviolet-visible transmittance of different fillers in DMF. (b) The resistance change–strain curves of AMGT conductive fibers with different filler contents. (c) The resistance change–time curves of the strain sensor under different loading and unloading stretches. (d) Durability test of the sensor under repeated 0–50% strains in 8000 cycles.

increase the intensity of the UV transmission spectrum at 400–800 nm.[30] As illustrated in Fig. 3a, when MWCNT : GE = 3 : 1, the intensity retention rate of transmitted light is the highest after 12 h or 48 h, indicating that it has the best dispersion effect in the solvent. Therefore, the mass ratio of MWCNTs and GE in the filler is set to 3 : 1. Moreover, the content of the filler affects the mechanical and electrical properties of the AMGT fiber. Fig. 3b shows the change in resistance ($\Delta R/R_0$) of the AMGT fiber with different mass fractions of the filler under strain. According to the definition, under the same strain, better conductivity stability results in a smaller $\Delta R/R_0$ value. It is observed that the $\Delta R/R_0$ value of these conductive fibers gradually increases with the stretching from 0% to 500%, and the increase rate increases significantly in the later stage. In the absence of MWCNT/GE fillers, the $\Delta R/R_0$ value changes the fastest under strain, and the $\Delta R/R_0$ reached 1000 at 310% strain. For conductive fibers containing 0.1 wt%, 0.5 wt% and 1.0 wt% MWCNT/GE fillers, the $\Delta R/R_0$ reaching 1000 corresponds to a strain of 336%, 446% and 322%, respectively. It is obvious that the $\Delta R/R_0$ of conductive fibers containing MWCNT/GE fillers will be smaller under strain. This is because the MWCNT/GE fillers are beneficial to bridge the separated AgNP islands, thus forming a more stable conductive network. In addition, the $\Delta R/R_0$ of the conductive fiber containing 0.3 wt% MWCNT/GE fillers changes the slowest under strain, and the $\Delta R/R_0$ is as low as 400 at 500% strain. The reason is that under the action of van der Waals force, excessive fillers will agglomerate in the TPU matrix with high viscosity, which will seriously hinder the electron transmission between fillers.[31,32] To make the AMGT fiber have good stretchability, the conductive fiber is prepared by adding 0.3 wt% MWCNT/GE fillers. Based on the high stretchability and conductivity, the AMGT fiber can still light up a small light-emitting diode (LED) at 100% strain (Fig. S5†). Therefore, the optimized AMGT fiber is used to develop a high-performance strain sensor.

Fig. 3c shows the response of the AMGT fiber strain sensor to cyclic stretching-releasing of different strains from 5% to 300%. The $\Delta R/R_0$ is very stable during the 5 stretching-releasing cycles, which indicates that the sensor has high reliability. The $\Delta R/R_0$ remains almost unchanged as the frequency increases from 0.25 to 2 Hz at 50% strain (Fig. S6†), so the sensor can meet the monitoring requirements of human motion at different frequencies. Moreover, as depicted in Fig. S7,† the fiber strain sensor showed a short response time of 47 ms and a fast recovery time of 68 ms, which was suitable for monitoring human movement signals. The stability and durability of the fiber sensor are the key to the practical application of wearable devices. Therefore, we performed stretching-releasing tests at 50% strain for 8000 cycles (Fig. 3d). The output curve maintains high consistency and repeatability, which fully demonstrates the excellent stability of the AMGT fiber strain sensor.

Fig. 4a shows the $\Delta R/R_0$ of the strain sensor under various strains, which can be divided into three different stages. First, in the low strain range of 0–220%, $\Delta R/R_0$ increases slowly because the conductive Ag shell on the fiber surface has not changed significantly. When the strain was further increased to 500%, a significant increase in $\Delta R/R_0$ was observed. Finally, in the large strain range from 500% to 600%, $\Delta R/R_0$ increases sharply. According to the SEM image, it can be seen that when the fiber is stretched to 550%, there are obviously many cracks in the Ag shell on the fiber surface. This leads to a decrease in the conductive path, and the resistance must increase rapidly. Obviously, this continuous and severe interruption of the partial conductive path will help the strain sensor to achieve high sensitivity (GF of 545). At the same time, under the tunneling-effect, the lower MWCNT/GE can bridge separated AgNP islands, which ensures the wide working range of the sensor (up to 600%). Fig. 4b plots a comparison of the stretchability and sensitivity between the AMGT fiber strain

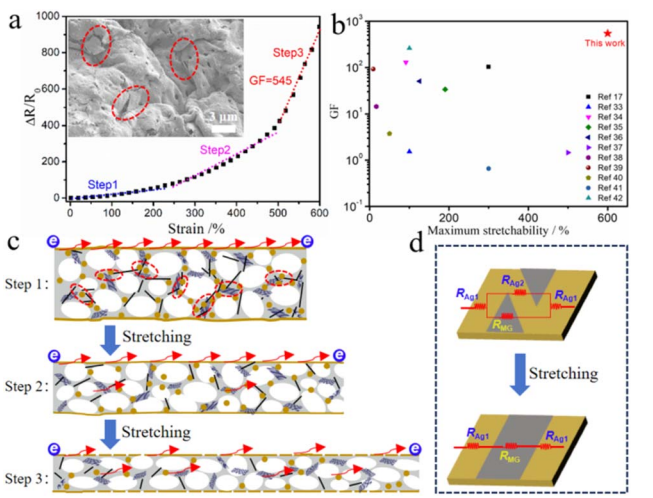

Fig. 4 (a) The resistance change–strain curve of the strain sensor and SEM image of the AMGT fiber at 550% strain. (b) Comparison of performance with other fiber strain sensors. (c) Schematic of the sensing mechanism of the strain sensor at different stages. (d) Resistance model of the sensor under different strains.

sensor and other reported fibre-based strain sensors.[17,33–42] It is visible that the designed AMGT fiber strain sensor with a synergistic three-dimensional conductive network exhibits a wide sensing range and high sensitivity, and will be a competitive candidate for strain sensing applications.

To understand the sensing mechanism of the strain sensor, we briefly describe the three stages in Fig. 4c. In addition, there are two ways to effectively transfer electrons to the conductive network during the whole stretching process, which can also be described vividly by using the resistance model in Fig. 4d. In the low strain range, the cracks are narrow and the neighboring Ag islands can still connect with each other. At this time, electrons tend to transfer along the Ag shell, and the total resistance of the conductive fiber can be calculated by using the following formula:[43,44]

$$R = \frac{2R_{Ag1}R_{Ag2} + 2R_{Ag1}R_{MG} + R_{Ag2}R_{MG}}{R_{Ag2} + R_{MG}}$$

where R_{Ag1}, R_{Ag2} and R_{MG} refers to the resistance of Ag islands, Ag bridge between two neighboring Ag islands, and MWCNT/GE below the Ag cracks, respectively. In the low strain stage, it can be assumed that the value of R_{Ag1} is basically unchanged. The increasing R_{Ag2} from crack propagation contributes the most to the increase in total resistance, and the effect of R_{MG} becomes more and more pronounced as its value approaches that of the rapidly increasing R_{Ag2}.[15] When the strain is further increased, the crack gap becomes larger and the lower MWCNT/GE layer begins to be responsible for electron transport to bridge the separate Ag islands. At this time, it is considered that R_{Ag2} is infinite, and the equation is approximately $R = 2RA_{g1} + R_{MG}$, which shows that the resistance increment under large strain comes from the future rupturing of Ag islands and the increase in tunneling resistance of the MWCNT/GE layer. In general, the synergistic effect of the crack-based Ag layer and tunneling effect-based MWCNT/GE layer makes the sensor have high sensitivity and a wide working range.

3.3. Application of strain sensors

This AMGT fiber strain sensor was able to work as a wearable device to monitor human movement in real-time. The strain sensor was attached to the skin of different parts of the human body to measure the pulse signal and joint bending under normal conditions, as observed in Fig. 5. As shown in Fig. 5a, the real-time pulse signal was recorded by the strain sensor. In particular, the three characteristic peaks of human pulse waveforms related to "P" (percussion), "T" (tide) and "D" (diastolic) can be clearly distinguished as each peak represents one pulse.[45] This result proves the superior sensitivity of our sensor. Additionally, our strain sensor can also be attached to the finger, elbow and knee to monitor finger joint bending, arm bending and gait characteristics (Fig. 5b–d). When a joint of the human body is bent repeatedly, the strain sensor can be bent in a periodical variation mode. In short, the sensor has high sensitivity and a wide working range, which is promising for applications in monitoring physiological and behavioral signals of the human body.

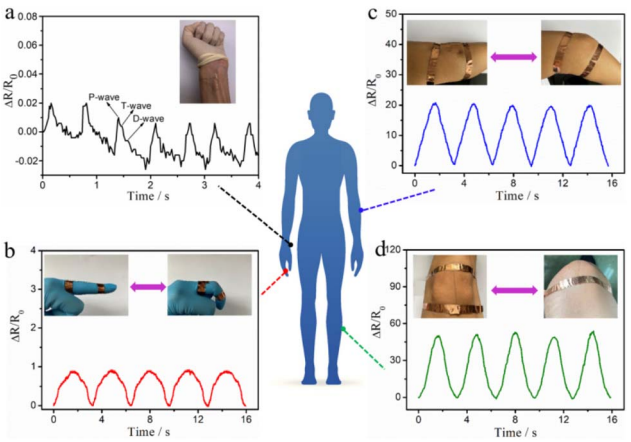

Fig. 5 Motion monitoring with the AMGT fiber strain sensor for various body positions: (a) pulse signal, (b) finger bending, (c) elbow bending and (d) knee bending.

4. Conclusions

In summary, we have developed a wide operating range and high-sensitivity fiber strain sensor based on a synergistic three-dimensional conductive network and crack propagation. The AMGT fiber with high initial conductivity (116 S cm^{-1}) was prepared by wet spinning and *in situ* reduction. Importantly, a synergistic three-dimensional conductive network was constructed in the conductive fiber, in which MWCNT/GE bridging separated AgNP islands ensures the integrity of the conductive pathway under large strains. The AMGT fiber strain sensor exhibits a wide sensing range of 600% and excellent stability (8000 cycles). At the same time, the crack propagation of the Ag shell on the fiber surface, makes the strain sensor have high sensitivity (GF of 545) under large strain. Furthermore, the application of the fiber strain sensor in real-time monitoring of various human motions is demonstrated, exhibiting great potential in the fields of personal healthcare and wearable devices.

Data availability

The authors declare that the all the data supporting the finding of this study are available within this article and its ESI files† and are available from the corresponding author on reasonable request.

Author contributions

Jianrong Yang and Wei Li: designed and supervised the research. Wei Shi: carried out material preparation, device fabrication, characterization, and wrote the manuscript. Xing Yang, Langhuan Lei, Xiaozhi Huang, Jiali Lin and Qiuyu Liang: helped in device fabrication, data collection, and discussion. All authors have read and agreed to the published version of the manuscript.

Conflicts of interest

There are no conflicts to declare.

Acknowledgements

This work was financially supported by the Natural Science Foundation of Guangxi Zhuang Autonomous Region (Grant No. 2024GXNSFBA010240), Guangxi Science and Technology Major Project (Grant No. GuikeAA22096018) and Guangxi Classification of Project (Grant No. GuikeAB22080094).

Notes and references

1 C. Chen, J. Feng, J. Li, Y. Guo, X. Shi and H. Peng, *Chem. Rev.*, 2023, **123**, 613–662.
2 M. Chen, J. Ouyang, A. Jian, J. Liu, P. Li, Y. Hao, Y. Gong, J. Hu, J. Zhou, R. Wang, J. Wang, L. Hu, Y. Wang, J. Ouyang, J. Zhang, C. Hou, L. Wei, H. Zhou, D. Zhang and G. Tao, *Nat. Commun.*, 2022, **13**, 7097.
3 K. K. Kim, M. Kim, K. Pyun, J. Kim, J. Min, S. Koh, S. E. Root, J. Kim, B.-N. T. Nguyen, Y. Nishio, S. Han, J. Choi, C. Y. Kim, J. B. H. Tok, S. Jo, S. H. Ko and Z. Bao, *Nat. Electron.*, 2023, **6**, 64–75.
4 Q. Su, Q. Zou, Y. Li, Y. Chen, S.-Y. Teng, J. T. Kelleher, R. Nith, P. Cheng, N. Li, W. Liu, S. Dai, Y. Liu, A. Mazursky, J. Xu, L. Jin, P. Lopes and S. Wang, *Sci. Adv.*, 2021, **7**, eabi4563.
5 M. Chen, P. Li, R. Wang, Y. Xiang, Z. Huang, Q. Yu, M. He, J. Liu, J. Wang, M. Su, M. Zhang, A. Jian, J. Ouyang, C. Zhang, J. Li, M. Dong, S. Zeng, J. Wu, P. Hong, C. Hou, N. Zhou, D. Zhang, H. Zhou and G. Tao, *Adv. Mater.*, 2022, **34**, 2200985.
6 L. Wang, X. Fu, J. He, X. Shi, T. Chen, P. Chen, B. Wang and H. Peng, *Adv. Mater.*, 2020, **32**, 1901971.
7 X. Song, J. Ji, N. Zhou, M. Chen, R. Qu, H. Li, L. a. Zhang, S. Ma, Z. Ma and Y. Wei, *Prog. Mater. Sci.*, 2024, **144**, 101288.
8 S. Chen, J. Li, H. Liu, W. Shi, Z. Peng and L. Liu, *Chem. Eng. J.*, 2022, **430**, 133005.
9 Y. Ding, J. Jiang, Y. Wu, Y. Zhang, J. Zhou, Y. Zhang, Q. Huang and Z. Zheng, *Chem. Rev.*, 2024, **124**, 1535–1648.
10 S. Akhavan, A. T. Najafabadi, S. Mignuzzi, M. A. Jalebi, A. Ruocco, I. Paradisanos, O. Balci, Z. Andaji-Garmaroudi, I. Goykhman, L. G. Occhipinti, E. Lidorikis, S. D. Stranks and A. C. Ferrari, *Adv. Mater.*, 2024, **36**, 2400703.
11 C. Ning, K. Dong, R. Cheng, J. Yi, C. Ye, X. Peng, F. Sheng, Y. Jiang and Z. L. Wang, *Adv. Funct. Mater.*, 2021, **31**, 2006679.
12 F. Lin, W. Li, X. Du, N. Chen, Y. Wu, Y. Tang and J. Jiang, *Appl. Surf. Sci.*, 2019, **493**, 1–8.
13 D. E. Camacho and A. Encinas, *Mater. Lett.*, 2021, **300**, 130204.
14 J. Lee, B. Llerena Zambrano, J. Woo, K. Yoon and T. Lee, *Adv. Mater.*, 2020, **32**, 1902532.
15 B. Niu, S. Yang, Y. Yang and T. Hua, *SmartMat*, 2023, **4**, e1178.
16 Q. Yu, J. Pan, Z. Jiang, Z. Guo and J. Jiang, *Chem. Eng. J.*, 2024, **493**, 152462.
17 Y. Yu, Y. Zhai, Z. Yun, W. Zhai, X. Wang, G. Zheng, C. Yan, K. Dai, C. Liu and C. Shen, *Adv. Electron. Mater.*, 2019, **5**, 1900538.
18 J. Zhou, X. Xu, Y. Xin and G. Lubineau, *Adv. Funct. Mater.*, 2018, **28**, 1705591.
19 C. Zhang, Q. Zhang, D. Zhang, M. Wang, Y. Bo, X. Fan, F. Li, J. Liang, Y. Huang, R. Ma and Y. Chen, *Nano Lett.*, 2021, **21**, 1047–1055.
20 Z. Xu, Z. Liu, H. Sun and C. Gao, *Adv. Mater.*, 2013, **25**, 3249–3253.
21 L. Sheng, T. Wei, Y. Liang, L. Jiang, L. Qu and Z. Fan, *Carbon*, 2017, **120**, 17–22.
22 H. Yuan, R. Jia, H. Yao, W. Wang, K. Qian, X. Wu, J. Li, Z. Wang, L. Lv, M. Han, Y. Dong and H. Wang, *Chem. Eng. J.*, 2023, **473**, 145251.
23 J. Wang, S. Liu, Z. Chen, T. Shen, Y. Wang, R. Yin, H. Liu, C. Liu and C. Shen, *J. Mater. Sci. Technol.*, 2025, **213**, 213–222.
24 X. Yue, C. Fang, Q. Yao, C. Liu, C. Shen and H. Liu, *Chem. Eng. J.*, 2024, **491**, 151853.
25 H. Sun, Y. Bu, H. Liu, J. Wang, W. Yang, Q. Li, Z. Guo, C. Liu and C. Shen, *Sci. Bull.*, 2022, **67**, 1669–1678.
26 J. Wang, H. Liu, X. Yue, D. Zhang, R. Yin, H. Sun, C. Liu and C. Shen, *Mater. Today Nano*, 2023, **24**, 100427.
27 S. Lee, S. Shin, S. Lee, J. Seo, J. Lee, S. Son, H. J. Cho, H. Algadi, S. Al-Sayari, D. E. Kim and T. Lee, *Adv. Funct. Mater.*, 2015, **25**, 3114.
28 W. Shi, S. Chen, Y. Lin, G. Zhang, Z. Peng, Z. Liu, H. Shi, X. Yan and L. Liu, *Chem. Eng. J.*, 2022, **441**, 136046.
29 Y. Yu, G. Zheng, K. Dai, W. Zhai, K. Zhou, Y. Jia, G. Zheng, Z. Zhang, C. Liu and C. Shen, *Mater. Horiz.*, 2021, **8**, 1037–1046.
30 X. Liu, G. Chen and C. Su, *J. Colloid Interface Sci.*, 2011, **363**, 84–91.
31 H. Liu, J. Gao, W. Huang, K. Dai, G. Zheng, C. Liu, C. Shen, X. Yan, J. Guo and Z. Guo, *Nanoscale*, 2016, **8**, 12977–12989.
32 K. Zhang, G.-H. Li, L.-M. Feng, N. Wang, J. Guo, K. Sun, K.-X. Yu, J.-B. Zeng, T. Li, Z. Guo and M. Wang, *J. Mater. Chem. C*, 2017, **5**, 9359–9369.
33 Y. Li, B. Zhou, G. Zheng, X. Liu, T. Li, C. Yan, C. Cheng, K. Dai, C. Liu, C. Shen and Z. Guo, *J. Mater. Chem. C*, 2018, **6**, 2258–2269.
34 Z. Li, X. Qi, L. Xu, H. Lu, W. Wang, X. Jin, Z. I. Md, Y. Zhu, Y. Fu, Q. Ni and Y. Dong, *ACS Appl. Mater. Interfaces*, 2020, **12**, 42179–42192.
35 B. Niu, T. Hua, H. Hu, B. Xu, X. Tian, K. Chan and S. Chen, *J. Mater. Chem. C*, 2019, **7**, 14651–14663.
36 H. Montazerian, A. Rashidi, A. Dalili, H. Najjaran, A. S. Milani and M. Hoorfar, *Small*, 2019, **15**, 1804991.
37 G. Chen, H. Wang, R. Guo, M. Duan, Y. Zhang and J. Liu, *ACS Appl. Mater. Interfaces*, 2020, **12**, 6112–6118.
38 Z. Liu, D. Qi, G. Hu, H. Wang, Y. Jiang, G. Chen, Y. Luo, X. J. Loh, B. Liedberg and X. Chen, *Adv. Mater.*, 2018, **30**, 1704229.
39 T. Huang, P. He, R. Wang, S. Yang, J. Sun, X. Xie and G. Ding, *Adv. Funct. Mater.*, 2019, **29**, 1903732.
40 J. Gao, Y. Fan, Q. Zhang, L. Luo, X. Hu, Y. Li, J. Song, H. Jiang, X. Gao, L. Zheng, W. Zhao, Z. Wang, W. Ai, Y. Wei, Q. Lu, M. Xu, Y. Wang, W. Song, X. Wang and W. Huang, *Adv. Mater.*, 2022, **34**, 2107511.

41 Z. Chen, H. Liu, X. Lin, X. Mei, W. Lyu and Y. Liao, *Mater. Horiz.*, 2023, **10**, 3569–3581.
42 H. Zhai, L. Xu, Z. Liu, L. Jin, Y. Yi, J. Zhang, Y. Fan, D. C. J. Li, X. Liu and Y. Li, *Chem. Eng. J.*, 2022, **439**, 135502.
43 C. Wang, X. Li, E. Gao, M. Jian, K. Xia, Q. Wang, Z. Xu, T. Ren and Y. Zhang, *Adv. Mater.*, 2016, **28**, 6640–6648.
44 W. Wang, Y. Ma, T. Wang, K. Ding, W. Zhao, L. Jiao, D. Shu, C. Li, F. Hua, H. Jiang, S. Tong, S. Yang, Y. Ni and B. Cheng, *ACS Appl. Mater. Interfaces*, 2022, **14**, 36611–36621.
45 F. Cai, C. Yi, S. Liu, Y. Wang, L. Liu, X. Liu, X. Xu and L. Wang, *Biosens. Bioelectron.*, 2016, **77**, 907–913.